



A natural molecule-driven organometallic conformal overlayer for high efficiency photoelectrochemical water splitting

Yuankai Li^a, Min-Cheol Kim^a, Chengkai Xia^b, Won Tae Hong^a, Jaekyum Kim^a, Geunsu Bae^c, Yoon Seo Jang^d, Se Yun Jeong^d, Eunji Sim^e, Chang Hyuck Choi^{c,f}, Tae-Hoon Kim^g, Ki Hyun Kim^{d,*}, Jung Kyu Kim^{a,h,**}

^a School of Chemical Engineering, Sungkyunkwan University (SKKU), 2066 Seobu-ro, Jangan-gu, Suwon, 16419, Republic of Korea

^b School of Materials Science and Engineering, North University of China, Taiyuan, Shanxi 030051, China

^c Department of Chemistry, Pohang University of Science and Technology, Pohang 37673, Republic of Korea

^d School of Pharmacy, Sungkyunkwan University, Suwon 16419, Republic of Korea

^e Department of Chemistry, Yonsei University, Seoul 03722, Republic of Korea

^f Institute for Convergence Research and Education in Advanced Technology (I-CREATE), Yonsei University, Seoul 03722, Republic of Korea

^g Department of Materials Science & Engineering, Chonnam National University, Gwangju 61186, Republic of Korea

^h SKKU Advanced Institute of Nanotechnology, Sungkyunkwan University (SKKU), Suwon 16419, Republic of Korea

ARTICLE INFO

Keywords:

Organometallic complex
Single atom
Cocatalyst overlayer
Water splitting
Green hydrogen

ABSTRACT

A surface manipulation of metal oxide-based photoelectrodes with overlaid co-catalysts has emerged as a promising strategy for boosting photoelectrochemical (PEC) water splitting activities. We demonstrate a nature molecule-mediated novel organometallic overlayer with exposed single atoms (SAs) on the surface of nano-particulate tungsten oxide (WO₃) photoanode with a significantly boosted solar water splitting activity and its long-term durability in aqueous electrolytes with wide pH range via a spontaneous one-pot assembly of a quercetin-nickel (QNi) complex on WO₃. The QNi complex with exposed Ni SAs modified WO₃ photoanode achieves a more than 2.7-fold enhancement on photocurrent density at 1.23 V_{RHE} in a mild condition (pH 7) and remarkable long-term durability of over 15 h. This work provides an attractive idea for efficient water splitting by utilizing a facile spontaneous assembly of organometallic overlayer with environmentally friendly materials, which is a step towards the goal of achieving green hydrogen.

1. Introduction

Hydrogen is considered as an ideal clean energy carrier because it has a high energy density and does not produce any greenhouse gases during combustion [1,2]. However, current commercial hydrogen production still relies on fossil fuels, which includes gray hydrogen production via a hydrocarbon reforming method, and is far from being sustainable [3]. In order to obtain green hydrogen with low energy consumption and without emission of pollution, solar water splitting is emerging at the forefront of current thinking. Photoelectrochemical (PEC) water splitting, which uses water as feedstock and transforms solar energy into green hydrogen, is considered as one of the promising technologies for sustainable energy [4,5]. For achieving clean PEC water splitting with high sustainability, transition metal oxides such as BiVO₄,

α-Fe₂O₃, and WO₃ are considered as candidate photoanode materials because of their earth-abundant, low-toxic, high water oxidation activity and their suitable band gap [6–10]. However, pristine metal oxides suffer from a low PEC performance, originating from sluggish catalytic kinetics and undesired photo-corrosion in highly acid/alkaline electrolyte solutions during the photo-assisted oxygen evolution reaction (OER) [11–16]. The low stability of pristine metal oxides in different pH environments limits their prospect for practical applications [17]. Furthermore, harsh pH-conditions on the PEC reaction of metal oxides leads to serious corrosion issues, which also restricts their versatile use for designing a commercial-cell setup [18–20].

Fabricating a cocatalyst overlayer on metal oxides is an effective approach to improve the catalytic kinetics and the stability of photoanodes [21–23]. Typical cocatalysts, including transition metal sulfides

* Corresponding author.

** Corresponding author at: School of Chemical Engineering, Sungkyunkwan University (SKKU), 2066 Seobu-ro, Jangan-gu, Suwon 16419, the Republic of Korea.

E-mail addresses: khkim83@skku.edu (K.H. Kim), legkim@skku.edu (J.K. Kim).

<https://doi.org/10.1016/j.apcatb.2023.123516>

Received 6 September 2023; Received in revised form 19 October 2023; Accepted 12 November 2023

Available online 15 November 2023

0926-3373/© 2023 Elsevier B.V. All rights reserved.

[24], nitrides [25], phosphides [26], and hydroxides [27–30] are known to be effective in restraining photo-corrosion and promoting charge-carrier migration, which can lead to an enhanced PEC water splitting activity [31,32]. These traditional cocatalysts are usually coated through various deposition techniques, such as chemical vapor deposition, spray coating, and photo/electrodeposition, however, they inevitably generate toxic or environmentally-harmful byproducts during the synthesis process [33]. Furthermore, the complete identification of the surface active sites is severely restricted by the irregularity and diversity of the cocatalyst in size and shape [34]. To fully meet the requirements of “green hydrogen”, it is necessary to develop eco-friendly, non-toxic cocatalysts based on plant-derived materials.

In response to this demand, quercetin-metal complexes can be attractive candidates for environmentally friendly cocatalysts because of their self-assembling, green manufacturing, and high catalytic activity [35]. Quercetin is a common secondary metabolite that belongs to a group of flavonoids known as the polyphenols [36]. It is widely distributed in nature and is also a basic ingredient of the human diet [36]. The richest source of quercetin is onion, one of the most popular vegetables, and various fruits and vegetables including mangoes, citrus fruits, plums, grapes, cherries, apples, and tomatoes are also sources of quercetin [37,38]. In addition, quercetin-metal complexes are reported to have strong oxidizing properties and can easily adsorb oxygen-containing functional groups. Therefore, attempts have been made to apply them in oxidative electrocatalytic processes such as glucose electrocatalysis and solar cell applications [39,40]. More importantly, owing to the unique structure of quercetin itself, the acidic protons-rich 3-hydroxy group provides the preferred adsorption sites for the metal ions, which makes it possible to achieve the exposed single-metal atoms (M-SAs) [40]. Since quercetin-metal complexes possess a high chemical stability and electrocatalytic activity, the introducing of this natural molecule-driven organometallic conformal overlayer onto metal oxide based catalysts for PEC water splitting is thoroughly attractive.

In this study, we assembled a natural molecule-driven organometallic quercetin-nickel (QNi) complex overlayer on the surface of nanoparticulate WO_3 photoanode, which enabled a stable and efficient PEC water splitting. This self-assembled conformal organometallic ultra-thin overlayer with exposed single Ni atoms outstandingly improved the efficiency of photo-induced charge transfer and prevented WO_3 from photo-corrosion during the PEC water splitting process in aqueous media. Furthermore, this firmly combined QNi overlayer with high chemical stability can prevent the irreversible conversion of acid-metal oxide WO_3 convert to tungstate in alkaline condition, which enables an efficient and stable PEC water splitting reaction in the wide pH range for the QNi/ WO_3 photoanode [41]. Density functional theory (DFT) simulation results illustrated that the QNi overlayer consists of a QNi complex stack, where planar QNi complexes are stacking with each other via face-to-face π - π stacking, forming an ordered hydroxyl binding group network that can strongly bind to the WO_3 surface. The conformal QNi complex ultra-thin overlayer promoted effective charge transfer at the electrolyte-semiconductor interface, thereby inhibiting the severe photo-corrosion of WO_3 in a neutral environment. Compared with a pristine WO_3 photoanode, QNi/ WO_3 showed significant improvement in the PEC OER performance and high stability in a neutral environment at pH 7. The simulations also demonstrated that the enhanced PEC OER kinetics of QNi/ WO_3 originates from the solar-driven OER reaction pathway on Ni SAs active sites of the QNi overlayer.

2. Experimental

2.1. Synthesis of the pristine WO_3 photoanode

A pristine WO_3 photoanode was synthesized on an F-doped SnO_2 -coated glass (FTO). First, the peroxy-tungstic acid precursor was formed by adding 9 g of tungsten powder in 10 mL of hydrogen peroxide

(H_2O_2 , Junsei). After that, 25 mL of IPA (2-propanol, Sigma Aldrich) and PEG 300 (poly(ethylene glycol) 300, Sigma Aldrich) were added into this solution to achieve improved stability and effectiveness of the porous nanostructures. The pristine WO_3 film on the FTO glass was fabricated according to the following procedure: (1) 20 μL of the peroxy-tungstic acid precursor was dropped coating on FTO glass (1.5 cm \times 1.5 cm) and, (2) dried at room temperature for 20 min, then (3) annealed at 550 $^\circ\text{C}$ for 2 h.

2.2. Synthesis of the QNi complex

The QNi complex was fabricated by the following method [42]. First, 0.01 M quercetin and 0.02 M nickel chloride (NiCl_2 , Sigma Aldrich) were dissolved in 20 mL methanol (CH_3OH , Sigma Aldrich). Then, 0.1 M NaOH-methanol solution was used to adjust the pH value to 10. The NaOH-methanol solution was prepared with 0.01 mol sodium hydroxide (NaOH, Sigma Aldrich) which was dissolved in 100 mL CH_3OH . Finally, the QNi complex solution was obtained after stirring the mixed solution for 2 h at room temperature.

2.3. Synthesis of the QNi/ WO_3 photoanode

150 μL of the QNi complex solution was uniformly dropped onto the as-synthesized WO_3 /FTO glass slide and dried for 30 min to completely volatilize the methanol solvent [43]. The final QNi/ WO_3 photoanode was obtained after the drop and vacuum drying for 12 h. Finally, flowing DI water was used to remove the residual powder on the samples which were then gently dried by N_2 gas purging. In order to study the catalytic mechanism of the QNi complex, carbon-nickel complex modified WO_3 (CNI/ WO_3) photoanodes were also synthesized as a reference. Furthermore, quercetin modified WO_3 (Q/ WO_3) photoanodes and NiCl_2 modified WO_3 (Ni/ WO_3) photoanodes were also synthesized. The detailed synthesis protocols for the references are listed in the [supplementary information](#).

2.4. Characterizations

Field emission scanning electron microscopy (FE-SEM, S-4700, Hitachi, Japan) and high-resolution transmission electron microscopy (HR-TEM, JEM ARM 200 F, JEOL, Japan) with an energy-dispersive X-ray spectroscopy (EDX) module were used to investigate the morphology of the samples. X-ray diffraction (XRD, Bruker D8 Discover, Germany, 40 kV, Cu K α radiation) and X-ray photoelectron spectroscopy (XPS, ESCALAB 250 spectrometer) were used to determine the crystalline structure and elementary constituents. Thermogravimetric analysis was measured by thermo gravimetry/differential thermal analyzer (TG/DTA6100, SEICO). The absorbance spectra were conducted by ultraviolet-visible spectroscopy (UV-vis, Shimadzu UV-3600). Fourier Transform-Nuclear Magnetic Resonance (NMR) spectroscopy were obtained using Unity Inova NMR 500 Hz. Fourier transform infrared (FT-IR) spectroscopy was obtained using Shimadzu IRTracer-100 spectrophotometer. Ni K-edge or W L $_3$ -edge X-ray absorption fine structure (XAFS) signals were obtained in the transmission or fluorescence mode at the Pohang Accelerator Laboratory (8 C, Nano XAFS). The corresponding metal foil was applied for the XAFS energy scale calibration. Athena and Artemis were used for X-ray absorption near edge structure (XANES) and extended X-ray absorption fine structure (EXAFS) analyses.

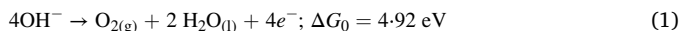
2.5. Photoelectrochemical measurements

PEC water splitting performances were conducted using a three-electrode configuration (reference 600 +, Gamry), the as-prepared photoanode, Pt wire and Ag/AgCl served as the working electrode, counter electrode and reference electrode, respectively (Hg/HgO was used in alkaline condition), 0.1 M KPi (pH 7), 0.05 M H_2SO_4 (pH 1) and

0.1 M NaOH (pH 13) were served as electrolytes in different pH conditions, respectively. Linear sweep voltammetry (LSV) tests were performed with a scan rate of 10 mV s⁻¹ under AM 1.5 G simulated 1 sun irradiation (150 W xenon lamp, PEC-L01, 100 mW cm⁻², Yokohama, Japan). The electrochemical impedance spectroscopy (EIS) was performed in the range of 100,000–0.1 Hz (1.23 V vs. RHE, 1 sun irradiation) with an amplitude of 5 mV. Mott–Schottky measurements were performed in dark condition (10 mV s⁻¹, 1000 Hz). 0.1 M Na₂SO₃ was served as hole scavenger to investigate the charge transfer/separation efficiency (η) of the samples. A gas chromatography was used to detect the O₂ evolution (three-electrode configuration, Young In Chromass).

2.6. Density functional theory calculations

DFT calculations were performed using the Gaussian 09 software package [44–48]. All calculations were carried out with the Minnesota 06 functional with 54% exact exchange (M06–2X) [49]. For the initial structure optimization and the torsional barrier calculations, the Karlsruhe basis set with valence triple-zeta and two sets of polarization functions (Def2-TZVPP), and the SMD solvation model, were utilized [50,51]. For the OER reaction mechanism calculation, all structures were optimized with the 6–31 + G* basis set due to the complexity of the system. The OER mechanism, under neutral conditions, is considered to follow the alkaline OER mechanism given by:



We assume reaction (1) proceeds in five elementary steps, as follows:



Here, we simulate the OER pathway on the Ni active site of the QNi complex since the QNi overlayer is more easily accessible than the WO₃ substrate. Reactions (3–6) follow the conventional OER mechanism, while the first deprotonation step, reaction (2), starts from the aqua ligand (*H₂O) on the QNi complex. Using the computational hydrogen electrode method, the reaction Gibbs free energies corresponding to Eqs. (2–6) can be expressed as [52,53]:

$$\Delta G_1 = E[*\text{OH}] - E[*\text{H}_2\text{O}] - E[\text{H}_2\text{O}] + 1/2E[\text{H}_2] + (\Delta\text{ZPE} - \text{T}\Delta\text{S})_1 - eU_{\text{RHE}} \quad (7)$$

$$\Delta G_2 = E[*\text{O}] - E[*\text{OH}] + 1/2E[\text{H}_2] + (\Delta\text{ZPE} - \text{T}\Delta\text{S})_2 - eU_{\text{RHE}} \quad (8)$$

$$\Delta G_3 = E[*\text{OOH}] - E[*\text{O}] - E[\text{H}_2\text{O}] + 1/2E[\text{H}_2] + (\Delta\text{ZPE} - \text{T}\Delta\text{S})_3 - eU_{\text{RHE}} \quad (9)$$

$$\Delta G_4 = E[*\text{O}_2] - E[*\text{OOH}] + 1/2E[\text{H}_2] + (\Delta\text{ZPE} - \text{T}\Delta\text{S})_4 - eU_{\text{RHE}} \quad (10)$$

$$\Delta G_5 = 2E[\text{H}_2\text{O}_{(\text{g})}] - 3/2E[\text{H}_2] + \Delta G_0 - E[*\text{O}_2] \quad (11)$$

where, E[A] is the DFT evaluated energy of species A, ($\Delta\text{ZPE} - \text{T}\Delta\text{S}$)_N is the zero-point energy and entropy difference between the product and reactants of reaction step N, and U_{RHE} is the potential of the electrode relative to the RHE [54]. Due to intrinsic errors in the DFT for describing the O_{2(g)} energy, the energy of O_{2(g)} is obtained from the formation energy of O₂ with respect to water ($E[\text{O}_{2(\text{g})}] = 2E[\text{H}_2\text{O}_{(\text{g})}] + \Delta G_0 - 2E[\text{H}_2]$). The OH⁻ energy is estimated from the chemical potential of OH⁻ with respect to the water ionization equilibrium potential [53]. U_{RHE} is calculated with respect to the standard hydrogen electrode (SHE) potential as [54]:

$$eU_{\text{RHE}} = eU_{\text{SHE}} + k_{\text{B}}T \times \text{pH} \times \ln 10 \approx eU_{\text{SHE}} + 0.059 \times \text{pH} \quad (\text{at } T = 298.15 \text{ K}) \quad (12)$$

We neglect the zero-point energy and entropy terms due to the computational cost of the frequency calculations on the QNi complexes.

3. Results and discussion

Fig. 1a schematically illustrates the synthesis protocol for the QNi/WO₃ photoanode. The nanoparticulated WO₃ film was first synthesized on the fluorine-doped tin oxide (FTO) coated glass using a facile sol-gel method [55]. Then, a QNi complex layer was conformally decorated on the photoanode surface by drop-coating at ambient temperature. The abundant acidic protons-rich 3-hydroxy group in quercetin molecules provide multiple sites for metal coordination. Therefore, quercetin molecules can self-assemble with nickel ions and form stable metal-phenolic networks [42,43,56–58]. Finally, a conformal QNi organometallic complex overlayer with exposed Ni SAs was decorated on the WO₃ photoanode via a facile spontaneous assembly process by dropping the QNi complex solution and drying its solvent in vacuum box.

The scanning electron microscopy (SEM) image of a QNi/WO₃ sample is shown in Fig. 1b. The nanoparticulate QNi/WO₃ film was composed of a mesoporous structure with the nanospheres (a diameter of around 70 nm), and its thickness was around 2 μm , as shown in the SEM cross-section image (Fig. S1a). No significant morphological differences were discovered among the SEM images of pristine WO₃ (Fig. S1b) and QNi/WO₃. The scanning transmission electron microscopy (STEM) images of QNi/WO₃ clearly show its hybrid structure (Fig. 1c and d), where an ultrathin QNi complex overlayer (2 nm) was conformally overlaid on the surface of WO₃ nanosphere for the QNi/WO₃ (Fig. 1c). The low or no crystallinity is also favorable for the conformal combination of quercetin-metal complexes on metal oxides [35]. The high angle annular dark field (HAADF) STEM image of QNi/WO₃ (Fig. 1d) clearly shows QNi organometallic complex overlayer. In Fig. 1e, energy dispersive X-ray (EDX) mapping images of QNi/WO₃ demonstrate that Ni-SAs are uniformly spread on the surface of the WO₃ nanosphere. EDX liner scanning analysis (Fig. 1f) also demonstrate that Ni only exists in the overlayer. The Ni distribution is consistent with the structural features of the distributed QNi organometallic complex overlayer observed in the HAADF images. Additionally, electron energy loss spectroscopy (EELS) analysis shown in Fig. 1g confirmed that the overlayer is composed of a nickel-based composite.

To study the role of the quercetin-nickel complex in the PEC OER, a carbon-nickel complex (CNI) was also synthesized as a reference. For this, the QNi complex was further carbonized at 500 °C in inert environment conditions. Thermogravimetric analysis was used to determine the synthesis temperature of the CNI complex. As shown in Fig. 2a, the carbonization temperature of the bare quercetin molecule is about 400 °C, and that of the quercetin-nickel complex is about 500 °C. Therefore, 500 °C was chosen as the synthesis temperature for the CNI complex to avoid the negative effect of high temperature on nickel elements. After the carbonization, a thinner overlayer was observed on the surface of the CNI-decorated WO₃ (CNI/WO₃) photoanode in the high-resolution transmission electron microscopy (HR-TEM) images (Fig. S2). X-ray diffraction (XRD) analysis was performed to reveal the crystallographic structures of WO₃, CNI/WO₃, and QNi/WO₃. The XRD patterns (Fig. 2b) of QNi/WO₃ and WO₃ show similar diffraction peaks, as indexed by the monoclinic WO₃ (JCPDS no. 43–1035). But after carbonizing at high temperature, the reflection peaks of CNI/WO₃ turned to broader state and shifted to lower angles, which is due to the carbon species diffusion in the WO₃ lattices [59].

X-ray photoelectron spectroscopy (XPS) was applied to analyze the valance and elemental compositions of the as-synthesized samples. The survey spectrum is shown in Fig. 2c. C=C peak at 284.6 eV of C 1 s spectrum was used to calibrate all XPS data. As shown in Fig. 2d, all

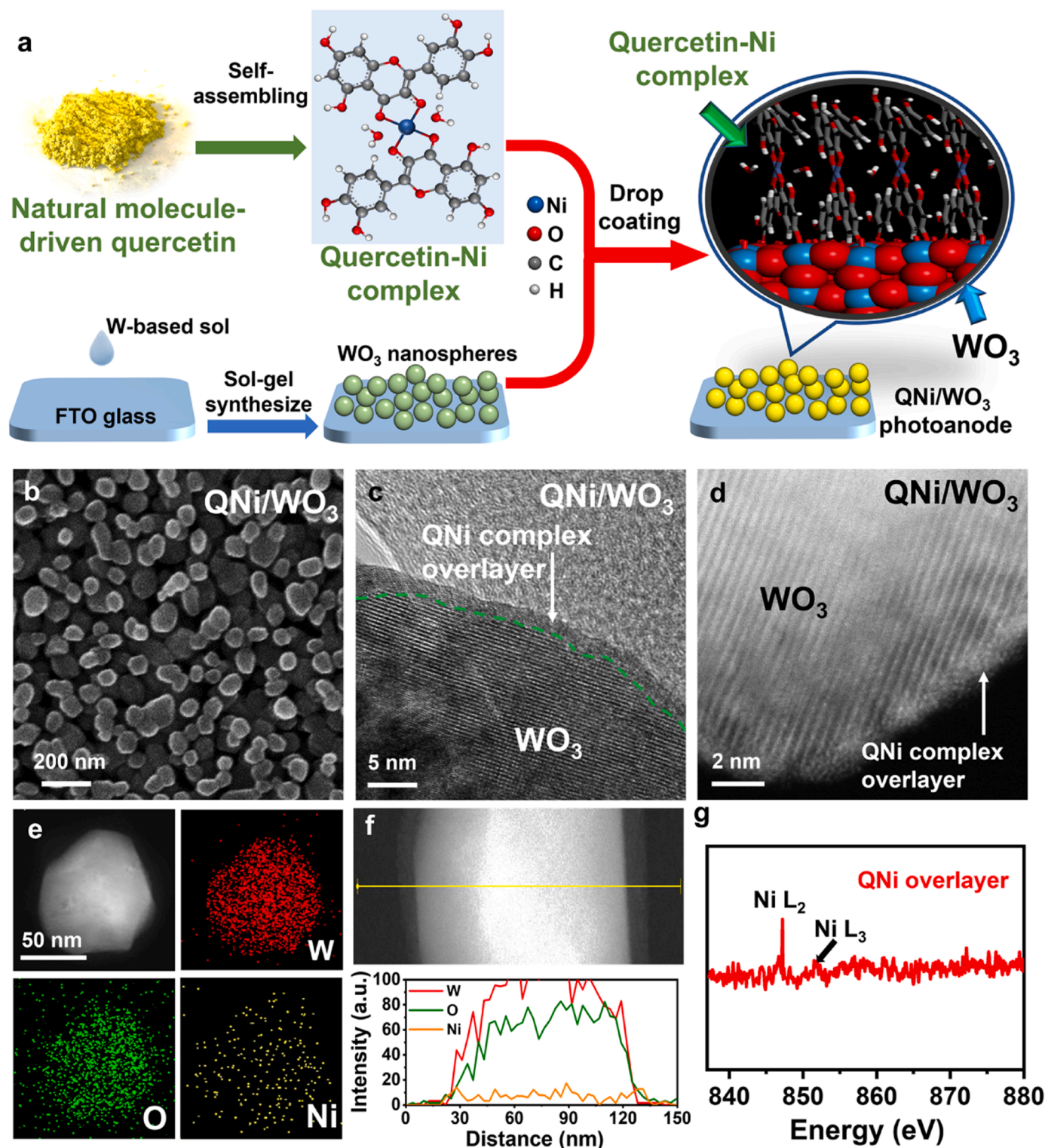


Fig. 1. Synthesis and morphology of the QNi/WO₃ photoanode. (a) Synthesis illustration of the QNi/WO₃ photoanode. (b) SEM image of QNi/WO₃ nanospheres. (c) TEM-BF image of QNi/WO₃ nanospheres. (d) HAADF-STEM images of QNi/WO₃ nanospheres. (e) EDS mapping of QNi/WO₃ nanospheres. (f) EDS liner scanning spectrum of QNi/WO₃ nanospheres. (g) EDS elemental spectra obtained from (c).

deconvoluted C 1 s spectra of the WO₃, CNi/WO₃, and QNi/WO₃ samples demonstrate three peaks which can be attributed to the standard sp² hybridized C=C, C-O, and O-C=O components, respectively [60]. Compared with pristine WO₃, QNi/WO₃ demonstrated higher intensity for the C-O-C peak, implying the presence of functional groups with C-O-C bonds in the QNi overlayer. In the C 1 s spectra of CNi/WO₃, the

peak intensity of C-O-C is close to that of pure WO₃, with an additional peak observed at 285.4 eV corresponding to the C-C bonding component. This indicates that the carbonization process removes the oxygen-containing functional groups in the quercetin-nickel complex and evolves into a carbon framework. Fig. 2e shows the W 4 f XPS spectra of the samples, where the deconvoluted peaks at 37.7 eV and

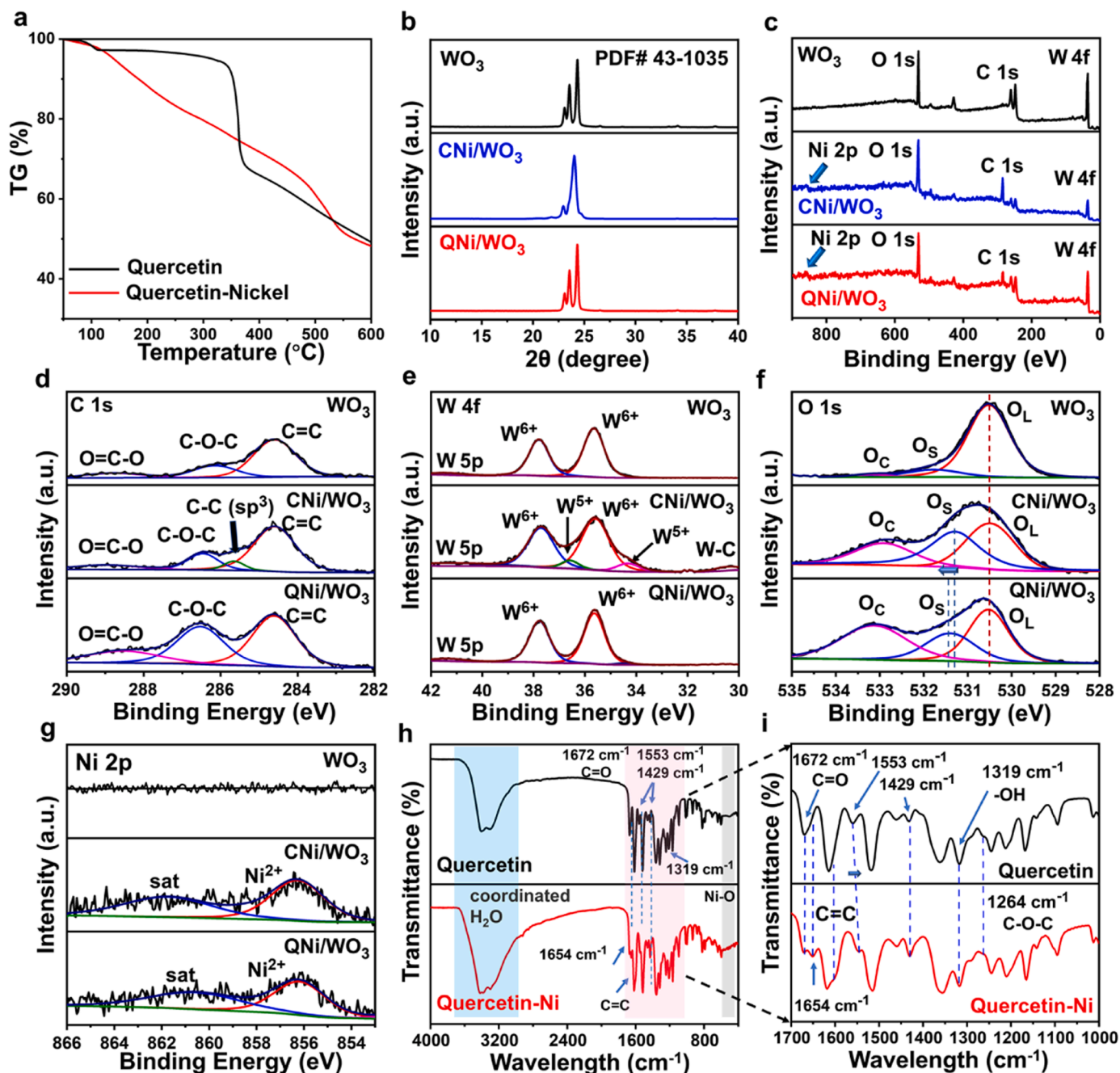


Fig. 2. Composition characterization of materials. (a) TG-DTA curves of quercetin powder and quercetin-Ni complex powder. (b) XRD patterns of WO₃, CNi/WO₃, and QNi/WO₃. (c-g) XPS spectrum of the survey spectrum, C 1 s, W 4 f, O 1 s, Ni 2p for WO₃, CNi/WO₃, and QNi/WO₃. (h and i) FT-IR spectra of quercetin and the quercetin-Ni complex.

35.6 eV can be attributed to W⁶⁺ [13]. Comparing to pristine WO₃, the spectrum of W 4 f of the QNi/WO₃ exhibits no change in the binding energy, suggesting combination of QNi complex and WO₃ doesn't change the crystalline structure of WO₃. Notably, in the W 4 f spectra of CNi/WO₃, the peak belongs to W⁵⁺ occurs at 36.5 eV and 34.2 eV, also, a deconvoluted peak ascribed to the W-C bond appears near 30.4 eV [61]. This indicates that some carbon atoms combined with tungsten atoms and generated a large number of oxygen vacancies after the carbonization process. For the O 1 s spectra shown in Fig. 2f, all the deconvoluted of the three samples exhibited three peaks at around 530.5 eV, 531.4 eV, and 533.1 eV, where the peaks at 530.2 eV are related to lattice oxygen (O_L) in WO₃, the peaks centered at 531.4 eV belong to surface absorbed oxygen (O_S) and peaks located at 532.9 eV

belong to chemically absorbed oxygen (O_C). Increased intensity was observed for the O_S and O_C peaks of QNi/WO₃, which indicates the existence of O-H and C=O bonding in the QNi complex [62]. The increased intensity for CNi/WO₃ at 531.6 eV is due to the oxygen vacancies generated in WO₃ after C and W atoms combined. The Ni 2p spectra (Fig. 2g) shows that after the carbonization, Ni 2p spectra slightly shifted to the higher valance state, indicates the oxidation of the Ni elements.

To clarify the molecular structure of the QNi complex, the coordination sites were investigated using Fourier transform infrared (FT-IR) spectroscopy, as shown in Fig. 2h and i. The structure of the quercetin molecule is given in Fig. S3. The characteristic stretching C=O mode of quercetin occurs at 1672 cm⁻¹, however, owing to the formation of the

QNi complex, this band shifted to 1654 cm^{-1} . This suggests that QNi coordination occurs through the carbonyl oxygen atom and the 3-OH or 5-OH group of the quercetin. In addition, the increased intensity of C-O at 1553 and 1429 cm^{-1} may be considered to be associated with the antisymmetric and symmetric stretching modes of the C-O group at the combination site [63]. The peak concentrated at 1319 cm^{-1} belongs to C-O-H and shows slightly decreased intensity, which can be attributed to metal combining with the -OH group on the B-ring of quercetin [31,64,65]. Further, the formation of metal complexes can be confirmed by the presence of ν (Ni-O) stretching vibration at the band around 500 cm^{-1} shown in Fig. S4, while no such band can be observed for quercetin. In addition, the ν (O-H) frequencies at around 3400 cm^{-1} are related to the presence of water [66–68]. When forming the QNi complex, the 4-oxo and 3-OH groups are the prioritized sites for involvement in the complexation process. In addition, as shown in Fig. 3a and b, the 3-OH group exhibits typical deprotonation behavior, which clearly demonstrates that the 3-OH functional group is the coordination site [69].

The physicochemical structure of W and Ni was then investigated using X-ray absorption fine structure (XAFS) spectroscopy. The W L_3 -edge X-ray absorption near-edge structure (XANES) and extended X-ray absorption fine structure (EXAFS) spectra of the WO_3 and QNi/ WO_3 samples are shown in Fig. 3c and d. In the XANES spectra, WO_3 and QNi/

WO_3 all exhibit a positive shift in adsorption edge and white line, compared to that of metallic W (ca. $+3.0\text{ eV}$; Fig. 3c), implying the fully oxidized state of W [70]. In contrast, the QNi/ WO_3 shows increased white line peak intensity compared to WO_3 , suggesting the higher tungsten occupied 5d states for the QNi/ WO_3 [71]. Their EXAFS spectra further reveal a W-O backscattering signal at 1.7 \AA , and W-W interaction appeared at 2.8 \AA (Fig. 3d). After identifying the insignificant change in the chemical nature of W in Ni complexes, this study further investigated the coordination structure of Ni SAs in the QNi complex at the Ni K-edge (Fig. 3e and f). Distinguishable from metallic Ni, its XANES spectrum contains an adsorption edge at 8345 eV (Fig. 3e) that corresponds to the average Ni oxidation state of ca. $+2.0$ (Fig. S5). In addition, the EXAFS spectrum of QNi shows a Ni-O backscattering signal at 1.9 \AA without Ni-Ni interaction at 2.4 \AA , suggesting the isolated Ni atoms in the QNi complex. (Fig. 3f and Fig. S6). The atomic Ni dispersion in the QNi complex can be further confirmed by the wavelet transforms (WT) of the EXAFS spectrum in k space (Fig. 3g and h). The WT-EXAFS of the QNi/ WO_3 exhibits a maximum intensity at 4.8 \AA^{-1} , related to the Ni-O coordination, while the maximum intensity at 7.5 \AA^{-1} corresponding to the Ni-Ni coordination is not detected. The Ni-O coordination is close to six, as shown in the QNi complex structure (Table S1), which is identical to the Ni coordination revealed by FT-IR and NMR analysis.

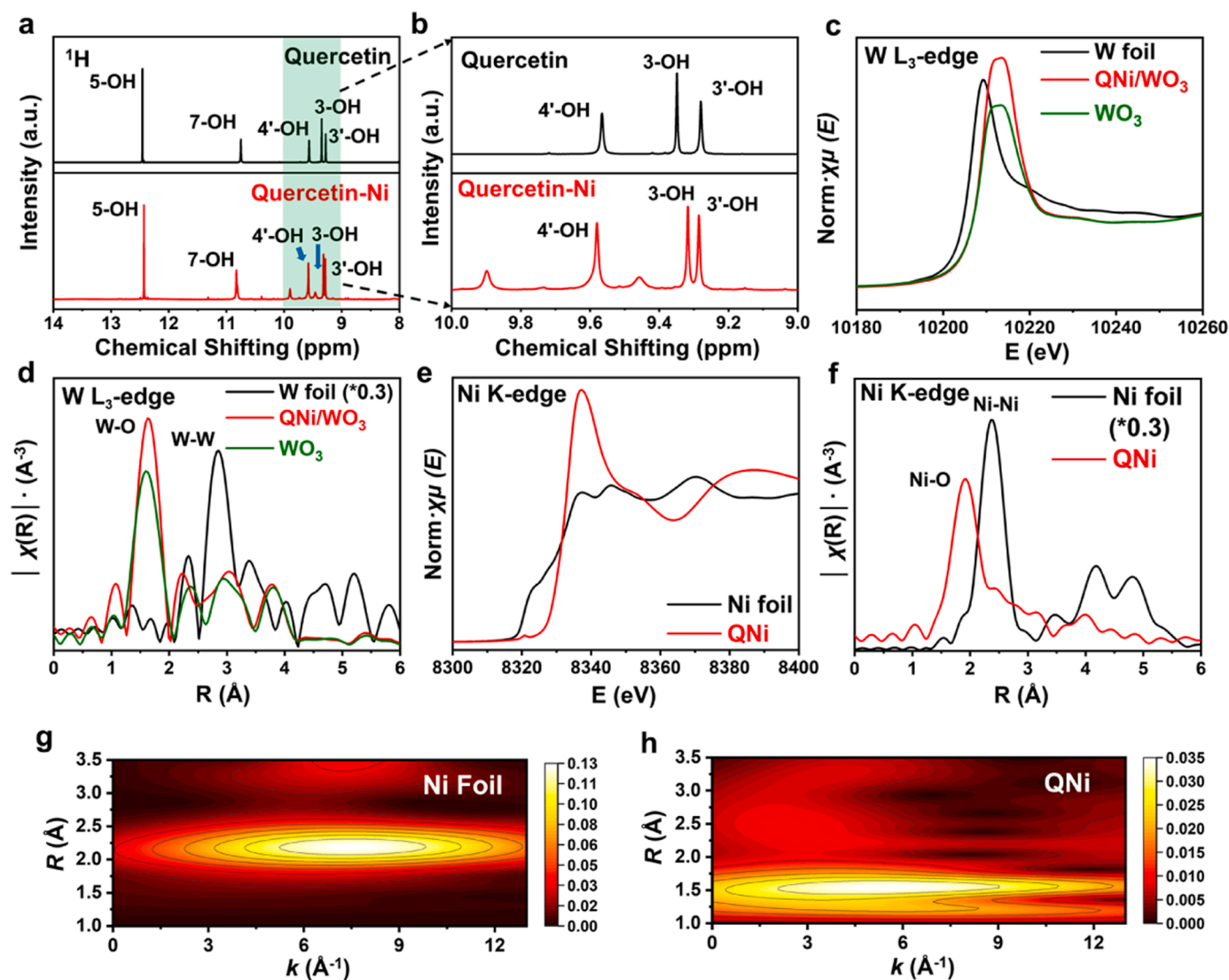


Fig. 3. Structure analysis of the quercetin-Ni complex. (a and b) ^1H NMR spectra of quercetin and the quercetin-Ni complex. (c and d) W L_3 -edge XANES and EXAFS spectra of QNi/ WO_3 and WO_3 . (e and f) Ni K-edge XANES and EXAFS spectra of quercetin-Ni complex. (g and h) WT-EXAFS of Ni Foil and quercetin-Ni complex.

It is noteworthy that the bare quercetin molecule or bare Ni precursor cannot spontaneously assemble with the WO_3 . In the STEM images of Q/WO_3 and Ni/WO_3 (Fig. S7), such an overlayer on the surface of the WO_3 nanospheres is not observed. To elucidate the reason why pristine quercetin does not bind to WO_3 while QNi complexes binds readily, DFT simulations were utilized to describe the molecular properties of the quercetin molecule and the QNi complex (Fig. 4). The structure optimization results indicate that there was a significant difference in the torsional angle between the biphenyl ring and the phenyl ring (ϕ) in the quercetin molecule ($\sim 30^\circ$) and the QNi complex ($\sim 0^\circ$). To further address this, the potential energy surface of the quercetin molecule and QNi complex was scanned with respect to ϕ . The most distinctive feature among the two molecular species is the torsional barrier around $\phi = 0^\circ$ (denoted as ϕ_0), where the torsional barrier at

ϕ_0 of the quercetin molecule (3.4 kJ mol^{-1}) is significantly higher than that of QNi (0.5 kJ mol^{-1}).

Note that the torsional barrier at ϕ_0 of quercetin is higher than the kinetic energy of ideal gas in 300 K (2.5 kJ mol^{-1}), while the ϕ_0 barrier of QNi is much lower. This indicates that ϕ of quercetin is "trapped" around 30° forming a non-planar aromatic structure, while ϕ of the QNi complex can reversibly rotate around $-15^\circ \sim 15^\circ$, forming a relatively planar aromatic structure compared to quercetin. The nonplanar aromatic structure of the quercetin molecule leads to unfavorable face-to-face π - π stacking among the molecules, while the planar aromatic structure of the QNi complex leads to favorable face-to-face π - π stacking among the aromatic rings (the face-to-face π - π stacking gets stronger with an increasing number of aromatic rings, while non-face-to-face aromatic ring interactions increase relatively slowly compared with

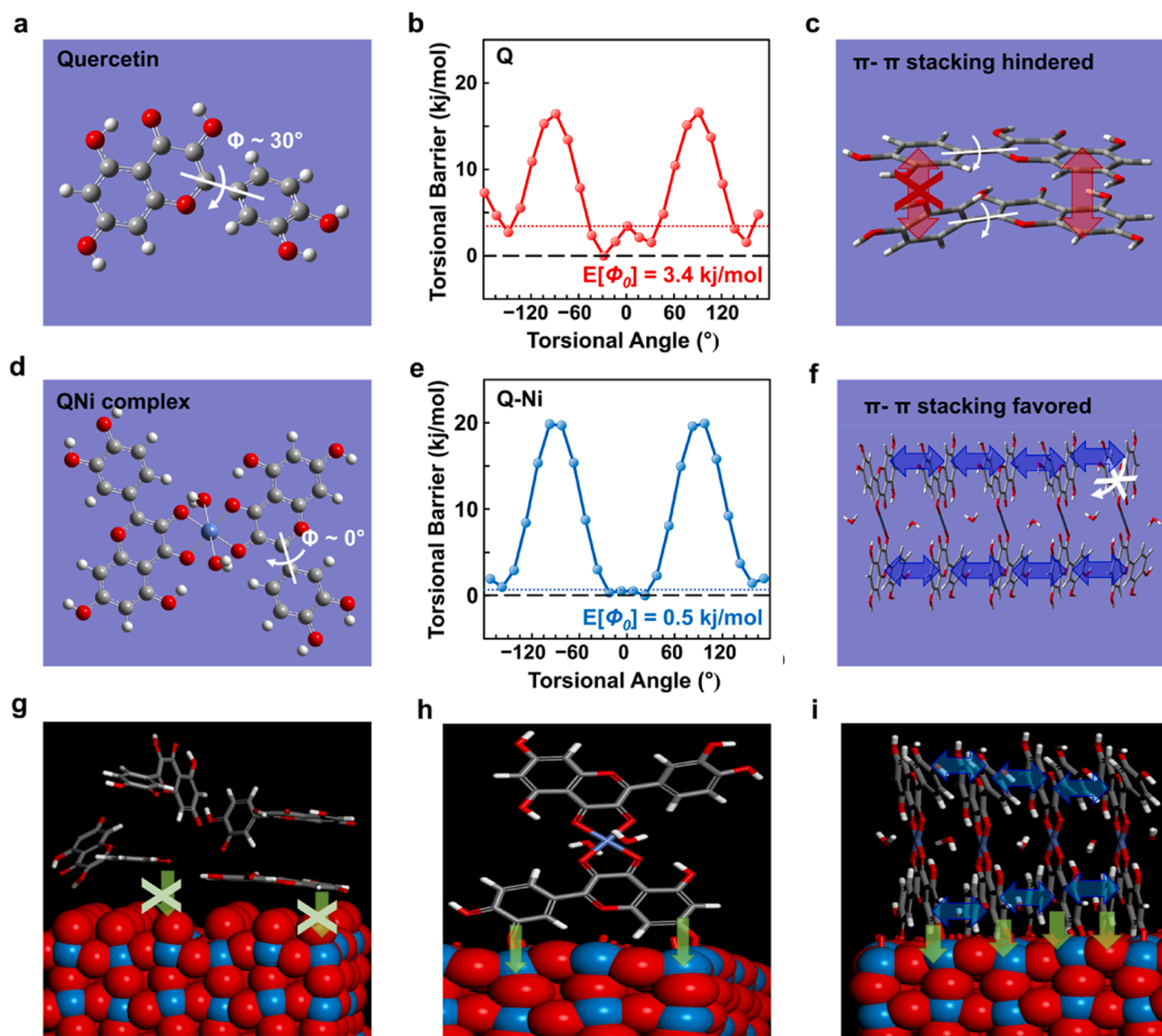


Fig. 4. DFT simulation for the QNi complex and WO_3 substrate combination. (a) DFT optimized molecular structure of quercetin. (b) Potential energy curve for the torsional rotation of quercetin. (c) π - π stacking is hindered due to the nonplanar aromatic structure of quercetin. (d) DFT optimized molecular structure of quercetin. (e) Potential energy curve for the torsional rotation of QNi. (f) π - π stacking is favored due to the relatively planar aromatic structure for QNi. Schematic diagram of the (g) Q/WO_3 system, and (h and i) the QNi/WO_3 system. The orientation of the binding of the hydroxyl groups in quercetin is randomly distributed due to the degree of freedom of the non-stacking molecules, while they are well-oriented towards WO_3 for well-stacked QNi complexes. For (b) and (e), the torsional barrier around $\phi = 0^\circ$ is depicted as a dotted line.

the face-to-face stacking with an increasing number of aromatic rings) [72]. As a consequence, the quercetin molecules have a higher degree of freedom in the solution than QNi, so the hydroxyl binding groups in quercetin are randomly oriented near the WO_3 surface, which makes it harder to bind with WO_3 . In contrast, QNi complexes can readily stack with each other, which aligns the hydroxyl binding groups in an ordered orientation, thus the stacked QNi complexes can easily bind with WO_3 .

The PEC and electrochemical properties of the as-synthesized WO_3 , CNI/WO_3 , and QNi/WO_3 samples were measured on an electrochemical workstation (three-electrode configuration, reference 600 +, Gamry), unless otherwise specified, all tests are performed in neutral condition (0.1 M KPi, pH 7). Before the PEC measurement, different volumes of QNi complex solution (50, 75, 100, 150, 175 and 200 μL) were introduced onto WO_3 to determine the optimized loading amount. The LSV curves shown in Fig. S8 (a) and corresponding statistics (Fig. S8 (b)) confirmed that the optimized loading amount would be 150 μL .

First, 50 cycles of cyclic voltammetry (CV) scan in dark condition were performed on the QNi/WO_3 sample for the surface activation

(Fig. S9). After that, linear sweep voltammetry (LSV) test under AM 1.5 G 1 sun illumination (100 mW cm^{-2}) was performed to evaluate the water splitting performance of WO_3 , QNi/WO_3 and CNI/WO_3 photoanodes. As shown in Fig. 5a, the pristine WO_3 photoanode yields a photocurrent density of 1.01 mA cm^{-2} at 1.23 V vs. RHE in a 0.1 M KPi aqueous electrolyte. After the decoration of the QNi complex overlayer on WO_3 , the corresponding value increased to 2.77 mA cm^{-2} , which is 2.7 fold higher than the bare WO_3 . However, CNI/WO_3 photoanode exhibits a dramatically decreased current density of 0.38 mA cm^{-2} . The onset potential of the J - V curve shown in Fig. 5b for QNi/WO_3 measured in dark was close to that of pristine WO_3 , while the onset potential of CNI/WO_3 was significantly decreased at around 500 mV. QNi and CNI complexes show different effects for improving the photoelectrochemical property of WO_3 . In addition, as shown in Fig. S10, we further applied the LSV test for WO_3 and QNi/WO_3 in different electrolyte while the pH value were 1 and 13 (0.05 M H_2SO_4 and 0.1 M NaOH, respectively). Fig. S10a illustrates that WO_3 has poor PEC response in the alkaline condition. In addition, the surface of WO_3 was

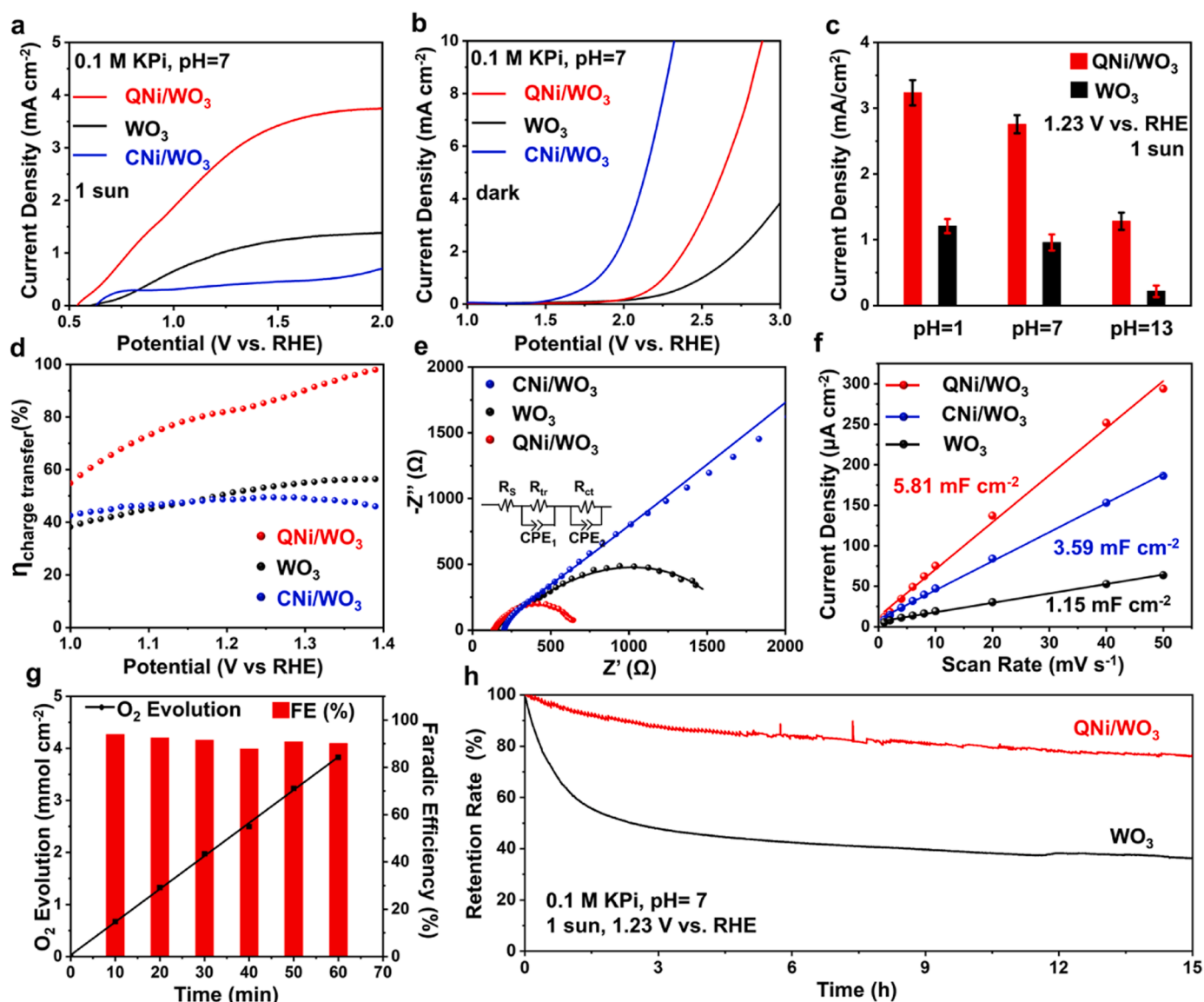


Fig. 5. Photoelectrochemical performance and properties. (a) LSV curves of WO_3 , CNI/WO_3 , and QNi/WO_3 measured in 0.1 M KPi (pH=7) under 1 sun illumination. (b) LSV curves of WO_3 , CNI/WO_3 , and QNi/WO_3 measured in dark conditions (0.1 M KPi, pH=7). (c) Statistics of the current densities of WO_3 and QNi/WO_3 at 1.23 V vs. RHE in different pH-conditions (pH=1, 7, 13) under 1 sun illumination, for each pH condition, 5 samples were synthesized and measured. (d) Charge transfer efficiency of WO_3 , CNI/WO_3 , and QNi/WO_3 . (e) Nyquist plot of WO_3 , CNI/WO_3 , and QNi/WO_3 in mild pH-conditions under 1 sun illumination. (f) ECSA of WO_3 , CNI/WO_3 , and QNi/WO_3 . (g) O_2 evolution-time plot of fabricated photoanodes. (h) Stability test of WO_3 and QNi/WO_3 photoanodes.

irreversibly damaged in the alkaline electrolyte, which resulted in very poor photocurrent response for the LSV test (Fig. S10b). Fig. S10c exhibits the LSV current density of QNi/WO₃ in different pH conditions, the corresponding statistics of the LSV current densities shown Fig. 5c illustrate that QNi/WO₃ achieves a higher average value of 3.23 mA cm⁻² in acid condition while in alkaline is 1.28 mA cm⁻². Importantly, the QNi complexes overlayer protects the WO₃ from direct corrosion by the NaOH electrolyte. Furthermore, after 15 h operation, the current density of QNi/WO₃ at 1.23 V vs. RHE under 1 sun still maintain more than 60% of the initial value (Fig. S10d), which implies that QNi/WO₃ enables pH-independent OER. Then Na₂SO₃ was served as hole scavenger to investigate the charge transfer efficiency ($\eta_{\text{charge transfer}}$) and transport characteristic of QNi/WO₃ (Fig. S11a). The $\eta_{\text{charge transfer}}$ of QNi/WO₃ at 1.23 V vs. RHE was significantly improved to be 86% compared to that of the pristine WO₃ 52%, while for the CNI/WO₃ was decreased to be 49% (Fig. 5d). The high $\eta_{\text{charge transfer}}$ demonstrates that the QNi complex overlayer outstandingly inhibits the surface charge recombination and boosts the surface catalytic activity, indicating that the QNi complex overlayer will provide favorable surface trap sites and accelerate the charge transfer process between electrode and electrolyte. Furthermore, based on the absorption photocurrent density (J_{abs}) obtained from light absorption (Fig. S11b) and photocurrent density tested with hole scavenger ($J_{\text{scavenger}}$), the charge transport efficiency ($\eta_{\text{transport}}$) of the three samples were calculated and shown in Fig. S11c ($\eta_{\text{transport}} = J_{\text{scavenger}}/J_{\text{abs}}$), at 1.23 V vs. RHE, $\eta_{\text{transport}}$ of pristine WO₃ and QNi/WO₃ were calculated to be 55% and 71%, respectively. However, the CNI/WO₃ value decreased to 14%, which was attributed to the combination of the carbon layer and WO₃.

Electrochemical impedance spectroscopy (EIS) test was carried out to study the reaction kinetics. EIS of WO₃, CNI/WO₃, and QNi/WO₃ was performed from 100 kHz to 0.1 Hz at 1.23 V_{RHE} under 1 sun illumination, the Nyquist plot is shown in Fig. 5e while the fitted parameters are provided in Table S2. The double semicircular curve of the Nyquist plot includes the electrolyte resistance (R_s), low-frequency charge transfer resistance (R_{ct}) and high-frequency charge transfer resistance (R_{cf}), where the ions diffusion in the low-frequency range within the electrode can be revealed by the vertical line of Nyquist plot. The calculated R_{ct} and R_{cf} parameters of QNi/WO₃ were 245 and 461 Ω , which were much smaller than those of CNI/WO₃ (1339 and 8231 Ω) and pristine WO₃ (424 and 1109 Ω). QNi/WO₃ has the lowest R_{cf} , which is consistent with the highest charge transfer efficiency it exhibited. Moreover, the EIS measured at 1.23 V vs. RHE in dark demonstrates the outstanding electrocatalytic activity of the fully carbonized CNI/WO₃ photoanode (Fig. S12). CNI/WO₃ has the lowest charge transfer resistance with 1313 Ω , which is lower than that of QNi/WO₃ and pristine WO₃. This indicates that the excellent electrical conductivity of fully carbonized materials can significantly improve the electrochemical activity of the material. However, the presence of C-W bonds and W⁵⁺ in the CNI/WO₃ XPS spectrum results in the combining of the carbonized layer, which leads to a large number of trap sites in CNI/WO₃, further aggravates the trapping of photogenerated holes under illumination. Thereby, CNI/WO₃ exhibits inferior photoelectrochemical water oxidation activity compared with QNi/WO₃ and WO₃. Furthermore, the electrochemical specific surface area (ECSA) was applied for further understanding of the electrocatalytic properties of as-synthesized photoanodes (Fig. S13). As illustrated in Fig. 5f, the C_{dl} values of pristine WO₃, CNI/WO₃, and QNi/WO₃ were 1.15, 3.59, and 5.81 mF cm⁻², respectively. The larger ECSA of QNi/WO₃ photoanode confirms the more active sites for the OER reaction, which results in higher electron transfer efficiency. As expected, under 1 sun illumination at 1.23 V_{RHE} in a three-electrode configuration, the QNi/WO₃ photoanode produced 2.01 $\mu\text{mol h}^{-1}$ cm⁻² of O₂ for 30 min, which is significantly higher than that of pristine WO₃ (0.98 $\mu\text{mol h}^{-1}$ cm⁻²) and CNI/WO₃ (0.53 $\mu\text{mol h}^{-1}$ cm⁻²) (Fig. 5g), the corresponding i-t curves of the samples are shown in Fig. S14a. The QNi/WO₃ photoanode achieves a Faradaic efficiency of 91.5% for O₂ evolution after 30 min, which is higher than that of WO₃

and CNI/WO₃ (Fig. S14b).

Chemical stability is another important issue when using an overlayer. As shown in Fig. 5h, after 15 h of testing at 1.23 V_{RHE} in a 0.1 M KPi electrolyte (pH 7) under 1 sun illumination, the QNi/WO₃ photoanode maintains its performance for about 80%. In contrast, the retention rate of WO₃ just maintain about 40% of its initial value. Additionally, the curves of CNI are always changing drastically during the stability test, which also indicates that the CNI complex overlayer is continuously undergoing violent redox reactions during the stability test. Fig. S15 shows the XRD patterns of QNi/WO₃ before and after the stability test, which illustrates no significant change on the crystal phase after long-term operation. Furthermore, the XPS spectra of the QNi/WO₃ before and after the long term stability test shown in Fig. S16 indicates the XPS results after long-term operation are similar to the spectrum obtained before the long-term stability test, which also indicates that the QNi complex overlayer is suitable for the long term PEC water oxidation reaction. The slight decrease of the O_{1s} peak and the increase in the intensity of the O_{2s} peak are related to the surface adsorption process of -OH during the reaction. The peaks of the carbon functional groups and Ni²⁺ remained stable after the stability test, indicating that the QNi complex overlayer can convert into NiOOH species and thereby suppress the photo-corrosion on the photoanode. As shown in the STEM images (Fig. S17), the QNi complex overlayer maintained its structure after 15 h operation in the PEC oxygen evolution test and remained conformally covered on the surface of WO₃ nanospheres without decomposition.

To gain insight into the enhanced water oxidation kinetics of the QNi/WO₃ catalyst, a mechanistic study with DFT simulations was performed for the OER process on the QNi/WO₃ catalyst. Modeling even a single QNi complex binding with the WO₃ surface is overly prohibitive in terms of computational cost, so a simplified QNi/WO₃ model was used based on the assumption that the Ni-SAs in the QNi complex are the OER active sites and the main role of WO₃ is to provide a photoelectrical bias to the QNi complex. The free energy diagram for the OER on QNi/WO₃ under dark and PEC conditions is shown in Fig. 6a. Under pH 7 and dark conditions with an applied bias of $U = 1.23$ V, QNi exerts a high overpotential (η) of 1.64 eV. This explains the relatively high onset potential of QNi under dark conditions. The decoration of QNi complex overlayer cannot change the bandgap position of bulk WO₃, but can affect the surface band energy state of the QNi/WO₃ [73,74]. Fig. 6b shows the Surface band energy diagram for QNi/WO₃ and WO₃, while the corresponding method to obtain the band energy diagram locations can be found in the Supporting information. For the PEC condition, a photo-voltage equal to the valence band edge of QNi/WO₃ was applied [75], which is evaluated as $U = 2.47$ V. Under the pH 7 and PEC conditions, the OER free energy diagram for QNi/WO₃ shows an overall downhill pathway. This OER pathway does not require any vacancy formation steps prior to the reaction, and the free energy for non-electrochemical O₂ gas desorption and H₂O molecule adsorption is nearly identical (0.3 eV), which makes the reaction more feasible. Overall, the PEC OER pathway shows that the WO₃ originated photovoltage greatly enhances the OER kinetics on the Ni-SAs active site of the QNi complex, which sufficiently explains the experimental findings.

4. Conclusion

In summary, the ultrathin conformal quercetin-nickel complex overlayer with exposed Ni-SAs was incorporated onto a nano-particulated WO₃ photoanode as a cocatalyst for long-durability and high-efficiency PEC water splitting in aqueous electrolytes with wide pH range. By passivating the WO₃ nanospheres with the QNi complex overlayer, the QNi/WO₃ photoanode shows a significantly boosted photocurrent density performance of 2.77 mA cm⁻² at 1.23 V_{RHE} in a 0.1 M KPi electrolyte (pH 7) under 1 sun illumination, which is more than 2.7 fold compared to that of pristine WO₃ (1.01 mA cm⁻²). The $\eta_{\text{charge transfer}}$ was outstandingly improved to 86% with the decoration of the QNi complex overlayer. In the result of the remarkably improved

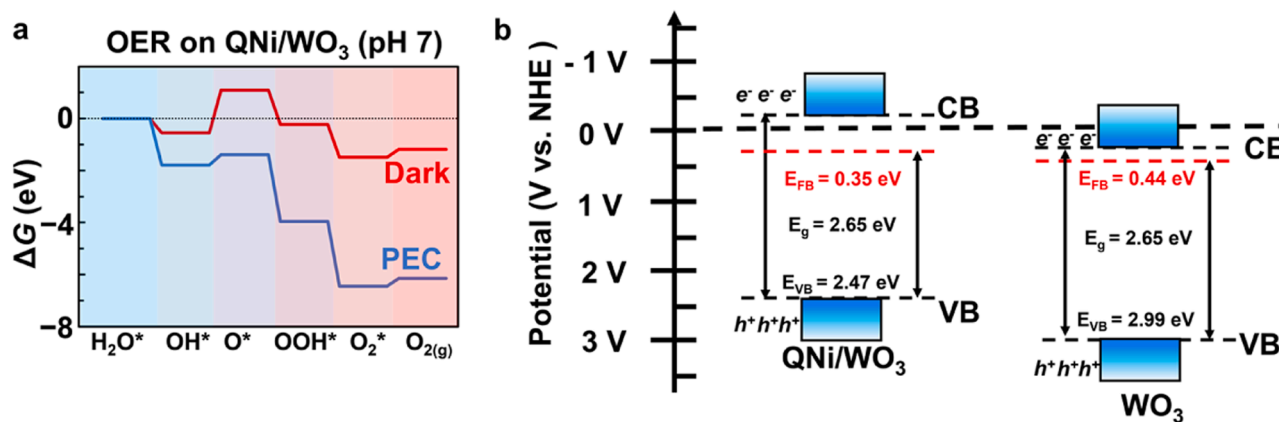


Fig. 6. DFT simulation for OER on QNi/WO₃. (a) Free energy diagrams of OER on QNi/WO₃ in dark and PEC conditions (pH 7) from DFT. (b) Surface band energy diagram for QNi/WO₃ and WO₃.

charge transfer property and the surface passivation effect to suppress the undesired photo-corrosion and surface degradation of WO₃ in neutral conditions, the QNi complex overlayer achieved long-term durability of the PEC OER for over 15 h under 1 sun illumination. The enhanced OER kinetics of QNi/WO₃ originates from the optimized PEC OER pathway on the Ni-SAs of the QNi overlayer and is promoted by the charge carrier migration from WO₃ to the Ni-SAs. This study provides new insight into green hydrogen production by utilizing non-toxic bio-based materials.

CRediT authorship contribution statement

Yuankai Li: Methodology, Investigation, Formal analysis, Writing - original draft. **Min-Cheol Kim:** Software, Formal analysis, Writing - original draft. **Chengkai Xia:** Conceptualization, Writing - original draft. **Won Tae Hong:** Investigation, Visualization. **Jaekyum Kim:** Data curation, Visualization. **Geunsu Bae:** Validation, Investigation. **Yoon Seo Jang:** Investigation. **Se Yun Jeong:** Investigation. **Eunji Sim:** Software. **Chang Hyuck Choi:** Resources, Validation, Investigation. **Tae-Hoon Kim:** Methodology, Validation. **Ki Hyun Kim:** Conceptualization, Supervision, Writing - review & editing. **Jung Kyu Kim:** Conceptualization, Supervision, Funding acquisition, Project administration, Resources, Writing - original draft, Writing - review & editing.

Declaration of Competing Interest

The authors announced that there is no financial/commercial conflict of interest.

Data Availability

Data will be made available on request.

Acknowledgements

Yuankai Li and Min-Cheol Kim contributed equally to this work. This work was supported by a National Research Foundation of Korea (NRF) grant funded by the Korean government (MSIT) (NRF-2022R1A2C1011559) and by the Korea Institute of Energy Technology Evaluation and Planning (KETEP) grant funded by the Korea government (MOTIE) (20214000000500, training program of CCUS for the green growth). Experiments at PLS-II were supported in part by MSIT and POSTECH.

Appendix A. Supporting information

Supplementary data associated with this article can be found in the

online version at [doi:10.1016/j.apcatb.2023.123516](https://doi.org/10.1016/j.apcatb.2023.123516).

References

- [1] C. Jiang, S.J.A. Moniz, A. Wang, T. Zhang, J. Tang, Photoelectrochemical devices for solar water splitting – materials and challenges, *Chem. Soc. Rev.* 46 (2017) 4645–4660, <https://doi.org/10.1039/C6CS00306K>.
- [2] A. Fujishima, K. Honda, Electrochemical photolysis of water at a semiconductor electrode, *Nature* 238 (1972) 37–38, <https://doi.org/10.1038/238037a0>.
- [3] L. Fulcheri, Y. Schwob, From methane to hydrogen, carbon black and water, *Int. J. Hydrog. Energy* 20 (1995) 197–202, [https://doi.org/10.1016/0360-3199\(94\)E0022-Q](https://doi.org/10.1016/0360-3199(94)E0022-Q).
- [4] B. You, Y. Sun, Innovative strategies for electrocatalytic water splitting, *Acc. Chem. Res.* 51 (2018) 1571–1580, <https://doi.org/10.1021/acs.accounts.8b00002>.
- [5] I. Roger, M.A. Shipman, M.D. Symes, Earth-abundant catalysts for electrochemical and photoelectrochemical water splitting, *Nat. Rev. Chem.* 1 (2017) 0003, <https://doi.org/10.1038/s41570-016-0003>.
- [6] H. Li, C. Lin, Y. Yang, C. Dong, Y. Min, X. Shi, L. Wang, S. Lu, K. Zhang, Boosting reactive oxygen species generation using inter-facet edge rich WO₃ arrays for photoelectrochemical conversion, *Angew. Chem. Int. Ed.* 135 (2022) 1, <https://doi.org/10.1002/anie.202210804>.
- [7] J. Ma, K. Mao, J. Low, Z. Wang, D. Xi, W. Zhang, H. Ju, Z. Qi, R. Long, X. Wu, L. Song, Y. Xiong, Efficient photoelectrochemical conversion of methane into ethylene glycol by WO₃ nanobar arrays, *Angew., Chem. Int. Ed.* 60 (2021) 9357–9361, <https://doi.org/10.1002/anie.202101701>.
- [8] J. Liu, W. Chen, Q. Sun, Y. Zhang, X. Li, J. Wang, C. Wang, Y. Yu, L. Wang, X. Yu, Oxygen vacancies enhanced WO₃/BiVO₄ photoanodes modified by cobalt phosphate for efficient photoelectrochemical water splitting, *ACS Appl. Energy Mater.* 4 (2021) 2864–2872, <https://doi.org/10.1021/acsaem.1c00145>.
- [9] Y. Liu, C. Xie, H. Li, H. Chen, Y. Liao, D. Zeng, Low bias photoelectrocatalytic (PEC) performance for organic vapour degradation using TiO₂/WO₃ nanocomposite, *Appl. Catal. B* 102 (2011) 157–162, <https://doi.org/10.1016/j.apcatb.2010.11.037>.
- [10] P. Shandilya, S. Sambyal, R. Sharma, P. Mandyal, B. Fang, Properties, optimized morphologies, and advanced strategies for photocatalytic applications of WO₃ based photocatalysts, *J. Hazard. Mater.* 428 (2022), 128218, <https://doi.org/10.1016/j.jhazmat.2022.128218>.
- [11] J. Knöppel, A. Kormányos, B. Mayerhöfer, A. Hofer, M. Bierling, J. Bachmann, S. Thiele, S. Cherevko, Photocorrosion of WO₃ photoanodes in different electrolytes, *ACS Phys. Chem. Au* 1 (2021) 6–13, <https://doi.org/10.1021/acspchemau.1c00004>.
- [12] C. Xia, Y. Li, M. Je, J. Kim, S.M. Cho, C.H. Choi, H. Choi, T.-H. Kim, J.K. Kim, Nanocrystalline Iron Pyrophosphate-Regulated Amorphous Phosphate Overlayer for Enhancing Solar Water Oxidation, *Nanomicro. Lett.* 14 (2022) 209, <https://doi.org/10.1007/s40820-022-00955-w>.
- [13] Y. Li, M. Je, J. Kim, C. Xia, S.H. Roh, W. So, H. Lee, D.-H. Kim, S.M. Cho, J.W. Bae, H. Choi, J.K. Kim, Rational nanopositioning of homogeneous amorphous phase on crystalline tungsten oxide for boosting solar water oxidation, *Chem. Eng. J.* 438 (2022), 135532, <https://doi.org/10.1016/j.cej.2022.135532>.
- [14] A. Kumar, V.Q. Bui, J. Lee, L. Wang, A.R. Jadhav, X. Liu, X. Shao, Y. Liu, J. Yu, Y.J. Nc Hwang, Moving beyond bimetallic-alloy to single-atom dimer atomic-interface for all-pH hydrogen evolution, *Nat. Commun.* 12 (2021) 1–10, <https://doi.org/10.1038/s41467-021-27145-3>.
- [15] Y.M. Choi, B.W. Lee, M.S. Jung, H.S. Han, S.H. Kim, K. Chen, D.H. Kim, T.F. Heinz, S. Fan, J. Lee, G.-R. Yi, J.K. Kim, J.H. Park, Retarded charge-carrier recombination in photoelectrochemical cells from plasmon-induced resonance energy transfer, *Adv. Energy Mater.* 10 (2020), 2000570, <https://doi.org/10.1002/aenm.202000570>.
- [16] J.K. Kim, X. Shi, M.J. Jeong, J. Park, H.S. Han, S.H. Kim, Y. Guo, T.F. Heinz, S. Fan, C.-L. Lee, J.H. Park, X. Zheng, Enhancing Mo:BiVO₄ solar water splitting with

- patterned au nanospheres by plasmon-induced energy transfer, *Adv. Energy Mater.* 8 (2018), 1701765, <https://doi.org/10.1002/aenm.201701765>.
- [17] J.C. Murillo-Sierra, A. Hernández-Ramírez, L. Hinojosa-Reyes, J.L. Guzmán-Mar, A review on the development of visible light-responsive WO₃-based photocatalysts for environmental applications, *Chem. Eng. J. Adv.* 5 (2021), 100070, <https://doi.org/10.1016/j.cej.2020.100070>.
- [18] X. Xiao, L. Yang, W. Sun, Y. Chen, H. Yu, K. Li, B. Jia, L. Zhang, T. Ma, Electrocatalytic water splitting: from harsh and mild conditions to natural seawater, *Small* 18 (2022), 2105830, <https://doi.org/10.1002/sml.202105830>.
- [19] J. Chen, C. Chen, M. Qin, B. Li, B. Lin, Q. Mao, H. Yang, B. Liu, Y. Wang, Reversible hydrogen spillover in Ru-WO_{3-x} enhances hydrogen evolution activity in neutral pH water splitting, *Nat. Commun.* 13 (2022) 5382, <https://doi.org/10.1038/s41467-022-33007-3>.
- [20] X. Zheng, M. Qin, S. Ma, Y. Chen, H. Ning, R. Yang, S. Mao, Y. Wang, Strong oxide-support interaction over IrO₂/V₂O₅ for efficient pH-universal water splitting, *Adv. Sci.* 9 (2022), 2104636, <https://doi.org/10.1002/adv.202104636>.
- [21] S. Tiwari, S. Kumar, A.K. Ganguli, Role of MoS₂/rGO co-catalyst to enhance the activity and stability of Cu₂O as photocatalyst towards photoelectrochemical water splitting, *J. Photochem. Photobiol. A* 424 (2022), 113622, <https://doi.org/10.1016/j.jphotochem.2021.113622>.
- [22] M. Arunachalam, D.-G. Lee, P.K. Das, K.R. Subhash, K.-S. Ahn, S.H. Kang, Surface engineering of Ba-doped TiO₂ nanorods by Bi₂O₃ passivation and (NiFe)OOH Co-catalyst layers for efficient and stable solar water oxidation, *Int. J. Hydrog. Energy* 47 (2022) 40920–40931, <https://doi.org/10.1016/j.ijhydene.2022.08.292>.
- [23] K. Jakubow-Piotrowska, B. Witkowski, J. Augustynski, Photoelectrocatalytic hydrogen generation coupled with reforming of glucose into valuable chemicals using a nanostructured WO₃ photoanode, *Commun. Chem.* 5 (2022) 125, <https://doi.org/10.1038/s42004-022-00745-w>.
- [24] L. Wang, W. Lian, B. Liu, H. Lv, Y. Zhang, X. Wu, T. Wang, J. Gong, T. Chen, H. Xu, A transparent, high-performance, and stable Sb₂S₃ photoanode enabled by heterojunction engineering with conjugated polycarbazole frameworks for unbiased photoelectrochemical overall water splitting devices, *Adv. Mater.* 34 (2022), 2200723, <https://doi.org/10.1002/adma.202200723>.
- [25] P. Wang, C. Ding, Y. Deng, H. Chi, H. Zheng, L. Liu, H. Li, Y. Wu, X. Liu, J. Shi, C. Li, Simultaneous improvement in hole storage and interfacial catalysis over Ni-Fe oxyhydroxide-modified tantalum nitride photoanodes, *ACS Catal.* 13 (2023) 2647–2656, <https://doi.org/10.1021/acscatal.2c06365>.
- [26] Y. Tao, Z. Ma, W. Wang, C. Zhang, L. Fu, Q. Zhu, Y. Li, G. Li, D. Zhang, Nickel phosphide clusters sensitized TiO₂ nanotube arrays as highly efficient photoanode for photoelectrocatalytic urea oxidation, *Adv. Funct. Mater.* 33 (2023), 2211169, <https://doi.org/10.1002/adfm.202211169>.
- [27] Y. Li, Q. Mei, Z. Liu, X. Hu, Z. Zhou, J. Huang, B. Bai, H. Liu, F. Ding, Q. Wang, Fluorine-doped iron oxyhydroxide cocatalyst: promotion on the WO₃ photoanode conducted photoelectrochemical water splitting, *Appl. Catal. B* 304 (2022), 120995, <https://doi.org/10.1016/j.apcatb.2021.120995>.
- [28] W. Fang, Y. Lin, R. Xu, L. Fu, Boosting photoelectrochemical performance of BiVO₄ photoanode by synergistic effect of WO₃/BiVO₄ heterojunction construction and NiOOH water oxidation cocatalyst modification, *ACS Appl. Energy Mater.* 5 (2022) 11402–11412, <https://doi.org/10.1021/acsaem.2c01869>.
- [29] Z. Kang, Z. Sun, Y. Zang, S. Wan, Y.-Z. Zheng, X. Tao, Dual functions of heterometallic FeCo oxyhydroxides in borate-treated BiVO₄ photoanodes toward boosted activity and photostability in photoelectrochemical water oxidation, *Chem. Eng. J.* 431 (2022), 133379, <https://doi.org/10.1016/j.cej.2021.133379>.
- [30] P. Wen, R. Lei, X. Cao, Q. Ma, G. Zhang, C. Guo, X. Wang, Y. Qiu, Anchored Ni nanocrystals boosting BiVO₄ photoanode for highly efficient water oxidation via in-situ generation of Ni@NiOOH co-catalyst, *Chem. Eng. J.* 454 (2023), 139983, <https://doi.org/10.1016/j.cej.2022.139983>.
- [31] J. Liang, M.-X. Wang, Y.-P. Zhao, W.-W. Yan, X.-G. Si, G. Yu, J.-P. Cao, X.-Y. Wei, Nano WO₃-Catalyzed One-Pot Process for Mild Oxidative Depolymerization of Lignin and its Model Compounds, *ChemCatChem* 13 (2021) 3836–3845, <https://doi.org/10.1002/cctc.202100670>.
- [32] C.X.M. Ta, Y. Furusho, F. Amano, Photoelectrochemical stability of WO₃/Mo-doped BiVO₄ heterojunctions on different conductive substrates in acidic and neutral media, *Appl. Surf. Sci.* 548 (2021), 149251, <https://doi.org/10.1016/j.apsusc.2021.149251>.
- [33] M. Kumar, B. Meena, P. Subramanyam, D. Suryakala, C. Subrahmanyam, Recent trends in photoelectrochemical water splitting: the role of cocatalysts, *NPG Asia Mater.* 14 (2022) 88, <https://doi.org/10.1038/s41427-022-00436-x>.
- [34] M.-M. Millet, G. Algara-Siller, S. Wrabetz, A. Mazheika, F. Girsig, D. Teschner, F. Seitz, A. Tarasov, S.V. Levchenko, R. Schlögl, E. Frei, Ni single atom catalysts for CO₂ activation, *J. Am. Chem. Soc.* 141 (2019) 2451–2461, <https://doi.org/10.1021/jacs.8b11729>.
- [35] X. Wang, Y. Fei, W. Wang, W. Yuan, C.M. Li, Polymer-mediated self-assembly of amorphous metal-organic complexes toward fabrication of three-dimensional graphene supported CoP nanoparticle-embedded n-doped carbon as a superior hydrogen evolution catalyst, *ACS Appl. Energy Mater.* 2 (2019) 8851–8861, <https://doi.org/10.1021/acsaem.9b01861>.
- [36] Deepika, P.K. Maurya, Health benefits of quercetin in age-related diseases, *Molecules* 27 (2022) 2498, <https://doi.org/10.3390/molecules27082498>.
- [37] T.L.A. Nguyen, D. Bhattacharya, Antimicrobial activity of quercetin: an approach to its mechanistic principle, *Molecules* 27 (2022) 2494, <https://doi.org/10.3390/molecules27082494>.
- [38] Q. Deng, X.X. Li, Y. Fang, X. Chen, J. Xue, Therapeutic potential of quercetin as an antiatherosclerotic agent in atherosclerotic cardiovascular disease: a review, *Evid. Based Complement. Altern. Med.* 2020 (2020), 5926381, <https://doi.org/10.1155/2020/5926381>.
- [39] Y. Shi, Y. Yu, Y. Liang, Y. Du, B. Zhang, In situ electrochemical conversion of an ultrathin tannin nickel iron complex film as an efficient oxygen evolution reaction electrocatalyst, *Angew. Chem. Int. Ed.* 58 (2019) 3769–3773, <https://doi.org/10.1002/anie.201811241>.
- [40] S. Çakar, M. Özacar, Fe-quercetin coupled different shaped ZnO rods based dye sensitized solar cell applications, *Sol. Energy* 155 (2017) 233–245, <https://doi.org/10.1016/j.solener.2017.06.017>.
- [41] Z. Chen, J. Li, S. Wang, J. Zhao, J. Liu, J. Shen, C. Qi, P. Yang, Structure-property-performance relationship of transition metal doped WO₃ mixed oxides for catalytic degradation of organic pollutants, *Chemosphere* 316 (2023), 137797, <https://doi.org/10.1016/j.chemosphere.2023.137797>.
- [42] J. Tan, L. Zhu, B. Wang, DNA binding and cleavage activity of quercetin nickel(ii) complex, *Dalton Trans.* 24 (2009) 4722–4728, <https://doi.org/10.1039/B901353A>.
- [43] H. Mutlu Gençkal, M. Erkisa, P. Alper, S. Sahin, E. Ulukaya, F. Ari, Mixed ligand complexes of Co(II), Ni(II) and Cu(II) with quercetin and diimine ligands: synthesis, characterization, anti-cancer and anti-oxidant activity, *J. Biol. Inorg. Chem.* 25 (2020) 161–177, <https://doi.org/10.1007/s00775-019-01749-z>.
- [44] R. Ditchfield, W.J. Hehre, J.A. Pople, Self-consistent molecular-orbital methods. IX. An extended Gaussian-type basis for molecular-orbital studies of organic molecules, *J. Chem. Phys.* 54 (1971) 724–728, <https://doi.org/10.1063/1.1674902>.
- [45] W.J. Hehre, R. Ditchfield, J.A. Pople, Self-consistent molecular orbital methods. XII. Further extensions of Gaussian-type basis sets for use in molecular orbital studies of organic molecules, *J. Chem. Phys.* 56 (1972) 2257–2261, <https://doi.org/10.1063/1.1677527>.
- [46] V.A. Rassolov, M.A. Ratner, J.A. Pople, P.C. Redfern, L.A. Curtiss, 6-31G* basis set for third-row atoms, *J. Comput. Chem.* 22 (2001) 976–984, <https://doi.org/10.1002/jcc.1058>.
- [47] T. Clark, J. Chandrasekhar, G.W. Spitznagel, P.V.R. Schleyer, Efficient diffuse function-augmented basis sets for anion calculations. III. The 3-21+G basis set for first-row elements, Li–F, *J. Comput. Chem.* 4 (1983) 294–301, <https://doi.org/10.1002/jcc.540040303>.
- [48] M.J. Frisch, J.A. Pople, J.S. Binkley, Self-consistent molecular orbital methods 25. Supplementary functions for Gaussian basis sets, *J. Chem. Phys.* 80 (1984) 3265–3269, <https://doi.org/10.1063/1.447079>.
- [49] Y. Zhao, D.G. Truhlar, The M06 suite of density functionals for main group thermochemistry, thermochemical kinetics, noncovalent interactions, excited states, and transition elements: two new functionals and systematic testing of four M06-class functionals and 12 other functionals, *Theor. Chem. Acc.* 120 (2008) 215–241, <https://doi.org/10.1007/s00214-007-0310-x>.
- [50] F. Weigend, R. Ahlrichs, Balanced basis sets of split valence, triple zeta valence and quadruple zeta valence quality for H to Rn: Design and assessment of accuracy, *Phys. Chem. Chem. Phys.* 7 (2005) 3297–3305, <https://doi.org/10.1039/B508541A>.
- [51] A.V. Marenich, C.J. Cramer, D.G. Truhlar, Universal solvation model based on solute electron density and on a continuum model of the solvent defined by the bulk dielectric constant and atomic surface tensions, *J. Phys. Chem. B* 113 (2009) 6378–6396, <https://doi.org/10.1021/jp810292n>.
- [52] J.K. Nørskov, J. Rossmeisl, A. Logadottir, L. Lindqvist, J.R. Kitchin, T. Bligaard, H. Jónsson, Origin of the overpotential for oxygen reduction at a fuel-cell cathode, *J. Phys. Chem. B* 108 (2004) 17886–17892, <https://doi.org/10.1021/jp047349j>.
- [53] Q. Liang, G. Brocks, A. Bieberle-Hütter, Oxygen evolution reaction (OER) mechanism under alkaline and acidic conditions, *J. Phys. Energy* 3 (2021), 026001, <https://doi.org/10.1088/2515-7655/abdc85>.
- [54] A. Bagger, I. Castelli, M. Hansen, J. Rossmeisl, Handbook of Materials Modeling: Applications: Current and Emerging Materials, Springer, Berlin, 2018, <https://doi.org/10.1007/978-3-319-44680-6>.
- [55] J.K. Kim, K. Shin, S.M. Cho, T.-W. Lee, J.H. Park, Synthesis of transparent mesoporous tungsten trioxide films with enhanced photoelectrochemical response: application to unassisted solar water splitting, *Energy Environ. Sci.* 4 (2011) 1465–1470, <https://doi.org/10.1039/C0EE00469C>.
- [56] W. Xu, S. Pan, B.B. Noble, J. Chen, Z. Lin, Y. Han, J. Zhou, J.J. Richardson, I. Yarovsky, F. Caruso, Site-selective coordination assembly of dynamic metal-phenolic networks, *Angew. Chem. Int. Ed.* 61 (2022), e202208037, <https://doi.org/10.1002/anie.202208037>.
- [57] A. Raza, X. Xu, L. Xia, C. Xia, J. Tang, Z. Ouyang, Quercetin-iron complex: synthesis, characterization, antioxidant, DNA Binding, DNA cleavage, and antibacterial activity studies, *J. Fluoresc.* 26 (2016) 2023–2031, <https://doi.org/10.1007/s10895-016-1896-y>.
- [58] M. Kalinowska, G. Świdorski, M. Matejczyk, W. Lewandowski, Spectroscopic, thermogravimetric and biological studies of Na(I), Ni(II) and Zn(II) complexes of quercetin, *J. Therm. Anal. Calorim.* 126 (2016) 141–148, <https://doi.org/10.1007/s10973-016-5362-5>.
- [59] M.S. Bazarjani, M.M. Müller, H.-J. Kleebe, C. Fasel, R. Riedel, A. Gurlö, In situ formation of tungsten oxycarbide, tungsten carbide and tungsten nitride nanoparticles in micro- and mesoporous polymer-derived ceramics, *J. Mater. Chem. A* 2 (2014) 10454–10464, <https://doi.org/10.1039/C4TA01509F>.
- [60] Y. Liu, J. Cao, A.V. Rogachev, A.A. Rogachev, I.I. Kontsevaya, X. Jiang, V. A. Yarmolenko, A.S. Rudenkov, M.A. Yarmolenko, D.L. Gorbachev, A.E. Pyzh, Low-energy electron beam deposition of coatings based on lignin and quercetin, their structure and properties, *Vacuum* 205 (2022), 111416, <https://doi.org/10.1016/j.vacuum.2022.111416>.
- [61] Y. Yang, X. Shao, S. Zhou, P. Yan, T.T. Isimjan, X. Yang, Interfacial electronic coupling of NC@WO₃-W₂C decorated ru clusters as a reversible catalyst toward

- electrocatalytic hydrogen oxidation and evolution reactions, *ChemSusChem* 14 (2021) 2992–3000, <https://doi.org/10.1002/cssc.202100893>.
- [62] M. Zeng, Y. Pan, W. Liu, J. Cui, Z. Lu, M. Zhu, A novel approach to the rapid in situ synthesis of tungsten carbide nanopowder by plasma milling and carbothermal reduction, *Adv. Eng. Mater.* 25 (2022), 2200175, <https://doi.org/10.1002/adem.202200175>.
- [63] S.B. Bukhari, S. Memon, M. Mahroof-Tahir, M.I. Bhangar, Synthesis, characterization and antioxidant activity copper–quercetin complex, *Spectrochim. Acta A Mol. Biomol. Spectrosc.* 71 (2009) 1901–1906, <https://doi.org/10.1016/j.saa.2008.07.030>.
- [64] S. Birjees Bukhari, S. Memon, M. Mahroof Tahir, M.I. Bhangar, Synthesis, characterization and investigation of antioxidant activity of cobalt–quercetin complex, *J. Mol. Struct.* 892 (2008) 39–46, <https://doi.org/10.1016/j.molstruc.2008.04.050>.
- [65] Y. Wang, C. Li, Y. Wan, M. Qi, Q. Chen, Y. Sun, X. Sun, J. Fang, L. Fu, L. Xu, B. Dong, L. Wang, Quercetin-loaded ceria nanocomposite potentiate dual-directional immunoregulation via macrophage polarization against periodontal inflammation, *Small* 17 (2021), 2101505, <https://doi.org/10.1002/sml.202101505>.
- [66] K. Shastrala, S. Kalam, K. Damerakonda, S.B.B. Sheshagiri, H. Kumar, R. Guda, M. Kasula, S.K. Bedada, Synthesis, characterization, and pharmacological evaluation of some metal complexes of quercetin as P-gp inhibitors, *Future J. Pharm. Sci.* 7 (2021) 99, <https://doi.org/10.1186/s43094-021-00252-0>.
- [67] D. Jeong, S. Sun, D. Moon, J. Cho, A functional model for quercetin 2,4-dioxygenase: geometric and electronic structures and reactivity of a nickel(II) flavonolate complex, *J. Inorg. Biochem.* 226 (2022), 111632, <https://doi.org/10.1016/j.jinorgbio.2021.111632>.
- [68] N. Podder, S. Mandal, The effects of metal cofactors on the reactivity of quercetin 2,4-dioxygenase: synthetic model studies with M(ii)-complexes (M = Mn, Co, Ni, Cu, Zn) and assessment of the regulatory factors in catalytic efficacy, *Dalton Trans.* 51 (2022) 17064–17080, <https://doi.org/10.1039/D2DT02853K>.
- [69] A. Primikyri, G. Mazzone, C. Lekka, A.G. Tzakos, N. Russo, I.P. Gerotheranassis, Understanding Zinc(II) chelation with quercetin and luteolin: a combined nmr and theoretical study, *J. Phys. Chem. B* 119 (2015) 83–95, <https://doi.org/10.1021/jp509752s>.
- [70] U. Jayarathne, P. Chandrasekaran, A.F. Greene, J.T. Mague, S. DeBeer, K. M. Lancaster, S. Sproules, J.P. Donahue, X-ray absorption spectroscopy systematics at the tungsten L-Edge, *Inorg. Chem.* 53 (2014) 8230–8241, <https://doi.org/10.1021/ic500256a>.
- [71] Q. Guan, C. Zhu, Y. Lin, E.I. Vovk, X. Zhou, Y. Yang, H. Yu, L. Cao, H. Wang, X. Zhang, X. Liu, M. Zhang, S. Wei, W.-X. Li, J. Lu, Bimetallic monolayer catalyst breaks the activity–selectivity trade-off on metal particle size for efficient chemoselective hydrogenations, *Nat. Catal.* 4 (2021) 840–849, <https://doi.org/10.1038/s41929-021-00679-x>.
- [72] S. Grimme, Do special noncovalent π – π stacking interactions really exist? *Angew. Chem. Int. Ed.* 47 (2008) 3430–3434, <https://doi.org/10.1002/anie.200705157>.
- [73] Y. Wang, H. Yin, X. Zhao, Y. Qu, A. Zheng, H. Zhou, W. Fang, J. Li, Photocatalytic ammonia synthesis from nitrate reduction on nickel single-atom decorated on defective tungsten oxide, *Appl. Catal. B* 341 (2024), 123266, <https://doi.org/10.1016/j.apcatb.2023.123266>.
- [74] Y. Zhao, W. Gao, S. Li, G.R. Williams, A.H. Mahadi, D. Ma, Solar- versus thermal-driven catalysis for energy conversion, *Joule* 3 (2019) 920–937, <https://doi.org/10.1016/j.joule.2019.03.003>.
- [75] Á. Valdés, Z.W. Qu, G.J. Kroes, J. Rossmeisl, J.K. Nørskov, Oxidation and photo-oxidation of water on TiO₂ surface, *J. Phys. Chem. C* 112 (2008) 9872–9879, <https://doi.org/10.1021/jp711929d>.